

## Analytical and Finite-Element Modeling of Resonant Silicon Microsensors

Thomas Fabula\* and Stephanus Büttgenbach<sup>1</sup>

Institut für Mikro- und Informationstechnik der Hahn-Schickard-Gesellschaft für angewandte  
Forschung e. V., Wilhelm-Schickard-Straße 10, D-78052 Villingen-Schwenningen, Germany

<sup>1</sup>Institut für Mikrotechnik der Technischen Universität Braunschweig,  
Langer Kamp 8, D-38106 Braunschweig, Germany

(Received June 12, 1995; accepted March 4, 1996)

**Key words:** finite-element modeling, resonant force sensors, resonant pressure sensors, modal analysis, electromechanical coupling factor, mode coupling, stress stiffening, piezoelectric thin films, triple-beam force sensor, 'beam-on-diaphragm' pressure sensor

This paper is concerned with the modeling of resonant silicon microsensors using analytical as well as finite-element methods. In the case of simple resonator structures, ideal boundary conditions and isotropic material properties, analytical methods can be used to model the dynamic behavior of resonant microsensors. For more complex resonator structures, arbitrary boundary conditions, anisotropic material properties, multi-layer structures, and in the presence of coupled-field effects, the finite-element method is well suited for simulating the behavior of resonant microstructures. Beamlike force and diaphragm pressure sensors are used to demonstrate the capability of this method to calculate eigenfrequencies, mode shapes, load-dependent frequency changes and cross-sensitivities as well as to optimize the resonator geometry with respect to mode selectivity, mode decoupling, electromechanical coupling efficiency, and measuring range and sensitivity. The numerical results are compared to experimental data in order to verify the finite-element models.

---

\*Present address: Deutsche Telekom AG, KSC Forschung & Entwicklung, D-53175 Bonn, Germany

## 1. Introduction

Resonant sensors, which change their output frequency as a function of the quantity to be measured, are attractive because of their high sensitivity, high resolution, and semi-digital output. Their operation is based on the fact that the frequency of acoustic waves in solids is a highly sensitive probe for parameters that alter the internal energy, the geometry or the boundary conditions of the resonating structure. In this paper we focus on silicon microsensors vibrating at their mechanical resonance frequency.<sup>(1-3)</sup> They are fabricated from single-crystal silicon using bulk micromachining technologies such as anisotropic wet etching and thin film deposition.<sup>(4)</sup>

For ideal boundary conditions, the dynamic behavior of simple resonator structures, for example, doubly clamped prismatic beams or all-around clamped flat diaphragms, may be modeled analytically with sufficient accuracy. In the case of arbitrary boundary conditions or of more complex resonator structures such as nonprismatic beams, 'butterfly' resonators,<sup>(5)</sup> 'H'-shaped resonators,<sup>(6)</sup> 'beam-on-diaphragm' structures,<sup>(7-10)</sup> or triple-beam<sup>(11)</sup> and quadruple-beam<sup>(12)</sup> resonators it is very difficult or even impossible to perform the analysis using analytical models. Instead, numerical methods such as the finite-element method<sup>(13)</sup> (FEM) can be used to study the behavior of such resonators and to enable efficient sensor design.

## 2. Principle of Resonant Silicon Microsensors

The general layout of a resonant pressure or force microsensor, which is resonated by piezoelectric thin films, is shown in Fig. 1. The resonant element consists of a silicon diaphragm or a beam. Piezoelectric thin films, for example zinc oxide (ZnO) layers,<sup>(14)</sup> are used to excite and detect the vibrations of the resonator, which is connected to the feedback loop of an oscillator circuit. The fabrication process<sup>(11)</sup> starts with the patterning and

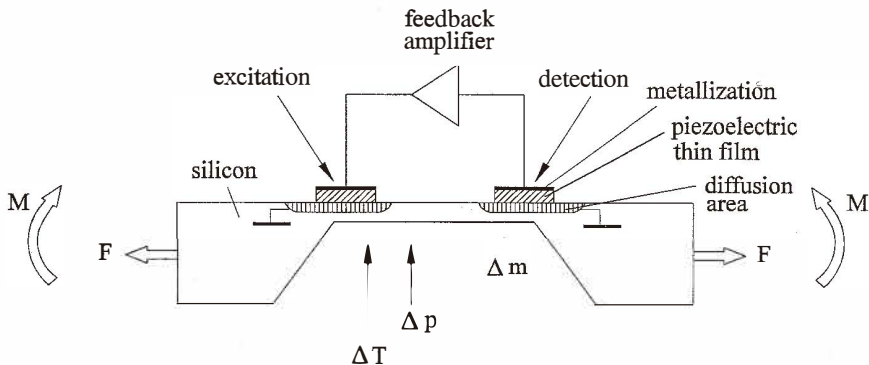


Fig. 1. General layout of a piezoelectrically driven resonant pressure or force microsensor.

doping of the ground electrode areas. In order to achieve a high electromechanical coupling efficiency, ZnO has to be grown with its *c*-axis perpendicular to the film plane and the silicon substrate. Well-oriented ZnO films may be deposited by r. f. sputtering from a Zn or ZnO target in an Ar/O<sub>2</sub> plasma. The ZnO is wet etched in a stirred solution of HAc, H<sub>3</sub>PO<sub>4</sub>, and H<sub>2</sub>O in order to form the piezoelectrically active regions. A sputtered and patterned Al metallization layer is used as the top electrode contact for the ZnO film. After completing the planar front-side process, anisotropic wet etching from the rear is applied to produce the desired beam or diaphragm thickness. In the case of beamlike resonators, in the final step deep trenching is performed by plasma etching the diaphragm from the front side.

Mechanical loading of the resonator due to a pressure difference  $\Delta p$  at the diaphragm or due to external forces  $F$  and moments  $M$  exerted on the beam results in tensile stress in the resonator element. Stress stiffening effects occur, which increase the stiffness of the resonator, thus changing its resonant frequency. Furthermore, a mass loading  $\Delta m$  or a temperature change  $\Delta T$  may lead to a frequency change. The output of the electronic oscillator circuit is fed to a frequency counter which records the load-dependent signal. The resonant microsensors considered in the following study are based on this principle; they consist of a passive resonator element and active elements for the excitation and detection of vibrations.

### 3. Analytical Description

Using methods such as modal analysis or Laplace transforms<sup>(15)</sup> the dynamic behavior of doubly clamped beams and all-around clamped flat diaphragms may be calculated analytically. Assuming homogeneous and isotropic material properties, the resonance frequencies, mode shapes, and load-dependent frequency changes can be calculated accurately.

#### 3.1 Beam resonators

The dynamic behavior of doubly clamped beam resonators can be described using a one-dimensional continuous analytical model. Assuming that the beam is prismatic and that its thickness  $t$  is much smaller than its width  $w$  and its length  $l$  (i.e.,  $l > w \gg t$ ) the following partial differential equation<sup>(16)</sup> describes the vertical displacements  $u(x,t)$ :

$$E'I \frac{\partial^4 u(x,t)}{\partial x^4} - F \frac{\partial^2 u(x,t)}{\partial x^2} + \rho A \frac{\partial^2 u(x,t)}{\partial t^2} + c \frac{\partial u(x,t)}{\partial t} = f(x,t). \quad (1)$$

This equation holds for small vibration amplitudes. The bending stiffness of the beam is given by  $E'I$ ,  $F$  is the axial force applied to the beam,  $\rho$  is the homogeneous mass density and  $A$  is the cross-sectional area. Beam damping is characterized by the viscous damping coefficient  $c$ .  $f(x,t)$  is a time- and position-dependent forcing function. The material behavior is assumed to be isotropic and is therefore described by the effective Young's

modulus  $E' = E/(1 - \nu^2)$ , where  $\nu$  is Poisson's ratio. For a doubly clamped beam, i.e.,  $u(x,t)|_{x=0,l} = 0$  and  $\partial u(x,t)/\partial x|_{x=0,l} = 0$ , the force-dependent frequency of the  $n$ -th natural mode is obtained from eq. (1) and may be approximated for the free, undamped case by<sup>(17)</sup>

$$f_n(F) \approx f_n(0) \sqrt{1 + \gamma_n \frac{FL^2}{12E'I}}, \quad (2)$$

where

$$f_n(0) = \frac{k_n^2}{2\pi} \sqrt{\frac{E'I}{\rho Al^4}} \quad (3)$$

and  $f_n(0) = f_n(F = 0)$ . The coefficients  $k_n$  and  $\gamma_n$  can be determined from the boundary conditions. For  $n \geq 3$  they are approximately given by  $k_n = \pi(n + 1/2)$  and  $\gamma_n = 12(k_n - 2)/k_n^3$ , and for  $n = 1, 2$  we have  $k_1 = 4.730$ ,  $k_2 = 7.853$ ,  $\gamma_1 = 0.295$ , and  $\gamma_2 = 0.145$ .

### 3.2 Diaphragm resonators

The static and dynamic behaviors of all-around clamped square diaphragms are described using Kirchhoff's and Love's plate and shell theories, assuming diaphragms whose thickness is very small compared to their lateral dimensions.<sup>(18)</sup> To calculate the eigenfrequencies and mode shapes, different approximation methods are used, for example the Rayleigh-Ritz method.<sup>(19)</sup> The resonance frequencies  $f_{ij}$  are given by<sup>(20)</sup>

$$f_{ij} = \frac{\lambda_{ij}^2}{2\pi\sqrt{12}} \frac{t}{a^2} \sqrt{\frac{E'}{\rho}}, \quad (4)$$

where  $a$  and  $t$  are the side length and thickness of the diaphragm, respectively, and  $i, j$  are the mode numbers. The constants  $\lambda_{ij}^2$  depend on the clamping conditions. Numerical values for  $\lambda_{ij}^2$ , taking into account the anisotropy of silicon, are given by Pons and Blasquez.<sup>(21)</sup> For the fundamental mode they obtained  $\lambda_{11}^2 = 35.16$ . For isotropic material properties the values of  $\lambda_{ij}^2$  are slightly higher than those for anisotropic properties, e.g.,  $\lambda_{11}^2 = 35.99$ .

The frequency change due to a transverse center displacement  $d$  of the diaphragm can be calculated from the general expression<sup>(22)</sup>

$$f(d) = f_0 \sqrt{1 + c \left(\frac{d}{t}\right)^2}, \quad (5)$$

where  $f_0 = f(d = 0)$ . The constant  $c$  depends on the clamping conditions, on the shape of the diaphragm, and on the vibration mode. For the fundamental mode of an all-around clamped square diaphragm, a value of  $c \approx 1.25$  was numerically estimated.<sup>(23)</sup>

For square diaphragms the relationship between the pressure  $p$  and the displacement  $d$

at the diaphragm center is implicitly given by<sup>(24)</sup>

$$p = 16E' \left( \frac{t}{a} \right)^4 \left[ 4.20 \left( \frac{d}{t} \right) + 1.58 \left( \frac{d}{t} \right)^3 \right]. \quad (6)$$

The frequency change due to pressure loading of the diaphragm is then derived by simultaneously solving eqs. (5) and (6).

### 3.3 Limitations of analytical methods

Analytical solutions to the boundary-value problems involving the static and dynamic behavior of resonant microsensors can be obtained only in special cases by assuming several idealizations as described above. The main disadvantage is that the exact boundary conditions cannot be accounted for, especially if the stiffnesses of the resonator and the clamping region are of the same order of magnitude. Furthermore, nonhomogeneous and anisotropic material properties as well as structured multilayer systems and distributed loads cannot be modeled.

## 4. The Finite-Element Method

As a general numerical approximation method, finite-element modeling facilitates the calculation of complex micromechanical resonators with arbitrary boundary conditions under the influence of nonlinear mechanisms. In addition, coupled-field effects such as electromechanical coupling can be accounted for. In the following we give an outline of the mathematical basis and program implementation. In section 5 the capabilities of this method are demonstrated with the help of several examples.

### 4.1 Equation of motion

The equation of motion for elastic solids can be derived using a variational approach such as the virtual work principle or Hamilton's principle.<sup>(25)</sup> The following differential equation, also called the 'stress-divergence theorem,' describes the static and dynamic behavior of a volume element  $d\Omega$  of an arbitrarily shaped elastic solid:

$$\rho \frac{\partial^2 u_i}{\partial t^2} = \sum_j \frac{\partial \sigma_{ij}}{\partial x_j} + F_i^\Omega \quad (i = 1,2,3), \quad (7a)$$

with the boundary condition at the surface

$$\sum_j n_j \sigma_{ij} = F_i^\Gamma \quad (i = 1,2,3), \quad (7b)$$

where  $u_i = x'_i - x_i$  is the  $i$ -th component of the displacement vector,  $\sigma$  is the stress tensor,

and  $\rho$  is the homogeneous mass density.  $F_i^\Omega$  and  $F_i^\Gamma$  are external volume forces and external stresses at the boundary, respectively, and  $n_i$  is the  $i$ -th component of the outward unit normal of a surface element  $d\Gamma$ . The stress tensor is related to the strain tensor  $\varepsilon$  by the stiffness tensor:  $\sigma_{ij} = \sum_{k,l} C_{ijkl} \varepsilon_{kl}$ .

The stress distribution and the displacements are obtained as solutions of eqs. (7a) and (7b). The displacements must be continuous functions with continuous partial derivatives up to the second order. Equations describing specific elastic systems such as doubly clamped beams (eq. (1)) or all-around clamped diaphragms can be derived from eqs. (7a) and (7b).<sup>(25)</sup>

#### 4.2 Weak formulation

In general, it is not possible to find closed-form analytical solutions to the elliptical boundary-value problem (eqs. (7a) and (7b), 'strong' formulation). Instead FEM uses a variational approach ('weak' formulation), which makes fewer demands on the smoothness of the solution. Approximation of the 'weak' solution is performed numerically by finite-element discretization.<sup>(26,27)</sup>

To obtain the 'weak' formulation, both sides of eq. (7a) must be multiplied by the displacements, which have partial derivatives of the first order and vanish on the clamped surface, and then integrated over the volume  $\Omega$  of the solid structure. By applying Green's theorem the partial derivatives of  $\sigma$  can be removed,<sup>(28)</sup> leading to:

$$\sum_{ij} \int_{\Omega} \varepsilon_{ij} \sigma_{ij} d\Omega = \sum_i \left\{ \int_{\Gamma} u_i F_i^\Gamma d\Gamma + \int_{\Omega} u_i \left( F_i^\Omega - \rho \frac{\partial^2 u_i}{\partial t^2} \right) d\Omega \right\}. \quad (8)$$

The numerical solution of eq. (8) can be determined by approximating the displacements  $u_i(x_1, x_2, x_3)$  at a given point  $(x_1, x_2, x_3)$  with a linear combination of a finite set of basis functions. These basis functions are the interpolation (or shape) functions  $N^k(x_1, x_2, x_3)$  of the elements, which divide the whole structure into finite subdomains connected by the nodes at the element edges. The coefficients  $u_i^k$  of the shape functions are the displacements at the nodes, i.e.,  $u_i(x_1, x_2, x_3) = \sum_k N^k(x_1, x_2, x_3) u_i^k$ , where the sum is over all nodes.<sup>(26)</sup>

#### 4.3 Program implementation

From eq. (8) one obtains the following matrix equation on an element level for static analyses:

$$[K] \cdot \{u\} = \{F\}, \quad (9)$$

where  $[K]$  is the stiffness matrix,  $\{u\}$  is the nodal displacement vector, and  $\{F\}$  is the vector of nodal mechanical forces. Due to geometric nonlinearities, the response of a microsensor varies disproportionately with the applied loads resulting in a change in the stiffness matrix  $[K]$  depending on the displacements:

$$[K(u)] \cdot \{u\} = \{F\}. \quad (10)$$

Finite-element programs are able to account for different types of nonlinearities. The effects relevant in this context are 'large deflection' and 'stress stiffening.'<sup>(29)</sup> Stress stiffening describes an increase in structural stiffness due to the stress state. Large deflection represents a change in stiffness resulting from a change in element spatial orientation as the microstructure deflects. This effect has to be taken into account especially for the simulation of diaphragms. The programs account for large deflection by updating the element orientations as the structure deflects and calculating an appropriate corrective load vector.<sup>(30)</sup> Since the stiffness is affected by the displacements, eq. (10) is solved iteratively using, for example, the Newton-Raphson method.<sup>(29)</sup>

Dynamic electromechanical coupled analyses are performed using piezoelectric state equations and by applying variational methods to obtain the coupled matrix equations on an element level:<sup>(31)</sup>

$$[M] \cdot \{\ddot{u}\} + [C] \cdot \{\dot{u}\} + [K_{uu}] \cdot \{u\} + [K_{u\phi}] \cdot \{\phi\} = \{F\} \quad (11)$$

$$[K_{\phi u}] \cdot \{u\} + [K_{\phi\phi}] \cdot \{\phi\} = \{Q\}. \quad (12)$$

In these coupled-field analyses the degrees of freedom at the nodes are the three components of the displacement vector and the electrical potential  $\phi$ .  $[M]$  is the mass matrix and  $[K_{uu}]$  is the structural stiffness matrix. Mechanical damping is described by the viscous damping matrix  $[C]$ , which is related to the mass and stiffness matrices by the Rayleigh damping coefficients:  $[C] = \alpha[M] + \beta[K_{uu}]$ . Electromechanical interaction is accomplished through the symmetrical piezoelectric coupling matrix  $[K_{u\phi}] = [K_{\phi u}]$  consisting of the piezoelectric moduli  $e_{ijk}$ . The dielectric conductivity matrix  $[K_{\phi\phi}]$  depends on the permittivity  $\epsilon_{ij}$ .  $\{Q\}$  is the vector of nodal electrical charges.

## 5. Numerical Modeling

The time required for the design and fabrication processes of microsensor devices can be considerably reduced by utilizing computer simulations. In addition, modeling provides a unique insight into the mode of operation of the devices. Numerical methods such as FEM are powerful tools for modeling the dynamic response of resonant sensors and for predicting the performance of microsensors under operating conditions. Geometry related effects, in particular, can be studied, for example, the optimization of clamping<sup>(32,33)</sup> and decoupling regions,<sup>(11,33)</sup> the calculation of the influence of various resonator cross-sectional shapes,<sup>(34)</sup> and the estimation of mode shapes of complex resonator structures. Furthermore, FEM is a valuable tool for the development of multilayer structures such as piezoelectrically driven microsensors and actuators.

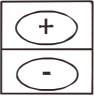
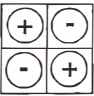
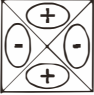
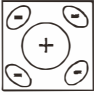
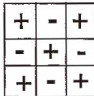
In the following, we report on the simulation of the static and dynamic behaviors of resonant force and pressure microsensors using the general-purpose finite-element code ANSYS.<sup>(35)</sup> Modal analysis was used to solve the eigenvalue problem and to determine the resonance frequencies and flexural mode shapes of beams, diaphragms, and complex resonator structures. The combination of static and subsequent modal analysis allows

calculation of the load-dependent frequency shifts. Utilizing this technique, the performance of resonant diaphragm pressure sensors has been optimized.<sup>(23)</sup>

### 5.1 Eigenfrequencies and mode shapes

Finite-element modeling was used to calculate the eigenvalues and mode shapes of a resonant pressure sensor consisting of a square silicon diaphragm  $50\ \mu\text{m}$  thick with sides  $9.2\ \text{mm}$  long covered with an approximately  $11\text{-}\mu\text{m}$ -thick ZnO thin film layer for piezoelectric excitation and detection. In Table 1 the numerical (FEM) results are compared to analytical and experimental ones. The resonance frequencies  $f_{ij}$  of the higher vibration modes are normalized by the frequency of the fundamental mode  $f_{11}$  ( $c_{ij} = f_{ij}/f_{11}$ ). The measurements were performed using piezoelectric excitation and optical detection of the vibrations. The analytical results agree well with the numerical ones (deviations of less than 4%). The influence of the anisotropic elastic material properties of silicon on the resonance frequencies is less than 4%. The measured values differ slightly from the results

Table 1  
Analytical, numerical (FEM), and experimental values of normalized frequencies  $c_{ij} = f_{ij}/f_{11}$  of a pressure sensor consisting of a square Si-ZnO-bimorph diaphragm resonator.

Vibration mode		Analytical results using eq. (4) and $\lambda_{ij}^2$ values from ref. 21		Numerical (FEM) results		Optical measurements
$ij$	Shape	Isotropic	Anisotropic	2D/isotropic	3D/anisotropic	
12		2.039	1.998	2.038	2.066	2.10
22		3.007	2.899	3.004	3.031	2.86
31		3.662	3.615	3.652	3.754	
13		3.679	3.631	3.669	3.770	3.94
33		6.122	5.872	6.105	6.021	6.35



calculated using a 3D, anisotropic finite-element model (deviations of less than 6%).

The main problem in calculating the resonance frequencies accurately arises from the unknown intrinsic stress of the ZnO thin films due to the compressive stress induced during the fabrication process. From the difference between the measured resonance frequency of the fundamental mode and the calculated value, the magnitude of the intrinsic stress can be estimated at about  $-15$  MPa.

### 5.2 Load-dependent frequency change

The diaphragm deflection due to pressure difference was calculated by performing a nonlinear analysis using the Newton-Raphson method and taking into account stress stiffening and large deflection effects. The static solution provides a load-dependent stiffness matrix for the sensor structure which is used in a subsequent modal analysis to determine the frequency shifts. Different finite-element models were used to investigate the influence of isotropic and anisotropic material behavior, different element types, solution methods, and boundary conditions. Model S43 uses 4-node 2D plastic shell elements (ANSYS element SHELL43). The material data were weighted by the layer thicknesses of silicon and ZnO, and ideal clamping of the diaphragm was assumed. The model V95 uses 20-node 3D solid elements (ANSYS element SOLID95). The material behavior was assumed to be isotropic for both silicon and ZnO and the real clamping geometry defined by the (111) silicon crystal planes was taken into account. Model V64 uses 8-node 3D solid elements (ANSYS element SOLID64). The material behavior was assumed to be anisotropic for both materials, and bulk data were taken from results reported by Landolt-Börnstein.<sup>(36)</sup>

Figure 2 shows the calculated and measured pressure-frequency characteristics for the fundamental flexural mode. The following parameter values have been measured: resonance frequency  $f_0 = 8317$  Hz, pressure sensitivity  $\Delta p/\Delta f \approx 12.4$  Hz/mbar, and maximum displacement at the center of the diaphragm  $d \approx 75$   $\mu\text{m}$ . The deviations of the measured values from the calculated ones are 2–7% for the resonance frequency, 5–19% for the diaphragm deflection, and up to 17% for the pressure sensitivity, indicating an extremely stiff model behavior. The parameter values calculated from eqs. (5) and (6) differ from the measured ones by 7% (resonance frequency), 12% (maximum diaphragm deflection), and 19% (pressure sensitivity).

The deviations of the measured values from the calculated ones are due to the intrinsic residual stress in the ZnO layer, the unknown material properties of thin film ZnO, which are influenced by technology-dependent parameters, and the nonhomogeneous diaphragm thickness resulting from the fabrication process.<sup>(37)</sup>

Further applications of dynamic finite-element simulations to resonant diaphragm pressure sensors and calculations of the effective electromechanical coupling factor for different sensor geometries and piezoelectric thin film materials are described elsewhere.<sup>(38,39)</sup>

### 5.3 Thermal behavior

Temperature changes strongly influence the properties of resonant microsensors. Besides the temperature dependence of the resonance frequency, buckling may occur in

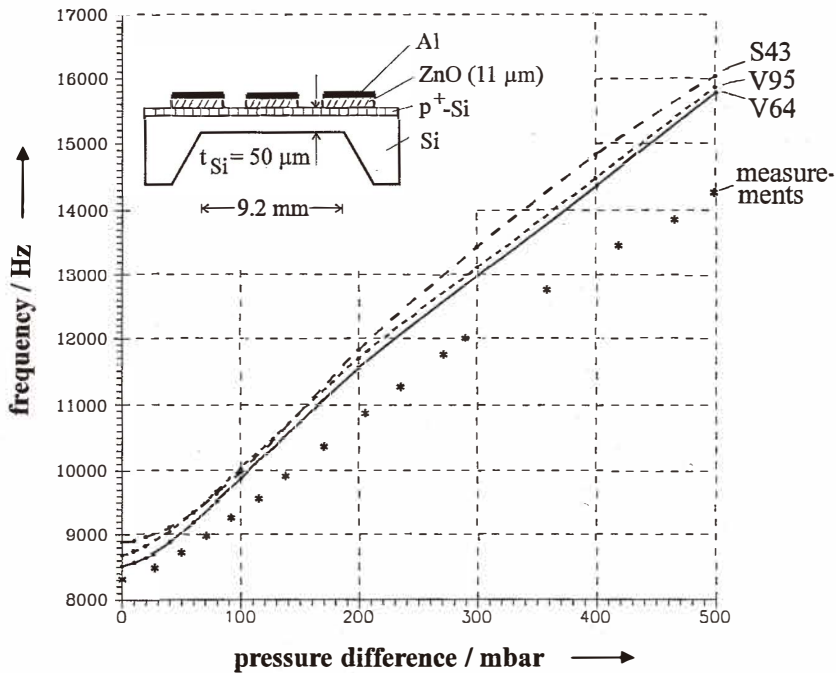


Fig. 2. Frequency-pressure characteristic of a piezoelectrically driven silicon diaphragm pressure sensor. The inset shows a schematic of the sensor. The calculations were performed assuming a silicon diaphragm covered with ZnO and neglecting the Al metallization layer. Model S43 uses 2D plastic shell elements, and models V95 and V64 3D solid elements.

doubly clamped beams and in diaphragms due to thermally induced compressive stress. The response of the resonance frequency to an axial load and the buckling stress for doubly clamped beams were studied by Bouwstra and Geijselaers.<sup>(17)</sup> The influence of temperature rise was investigated by Geijselaers and Tjeldeman<sup>(40)</sup> who used an approximate analytical model as well as finite-element simulation to characterize the dynamic behavior of a resonating mass-flow sensor.

The analytical model of Geijselaers and Tjeldeman<sup>(40)</sup> and 2D and 3D finite-element models were used to calculate the temperature-dependent characteristics of a doubly clamped beam resonator accounting also for the temperature drop due to heat transfer to a passing mass flow.<sup>(41)</sup>

In order to verify the numerical results, optical and electrical measurements were performed on a doubly clamped silicon beam with a length of 10 mm and a thickness of 50  $\mu\text{m}$ , from which the resonance frequencies and static buckling amplitudes were estimated. The beam was forced to vibrate by thermal excitation via metal thin film resistors (see inset in Fig. 3). Electrical detection was achieved using thin film strain gauges, while for optical

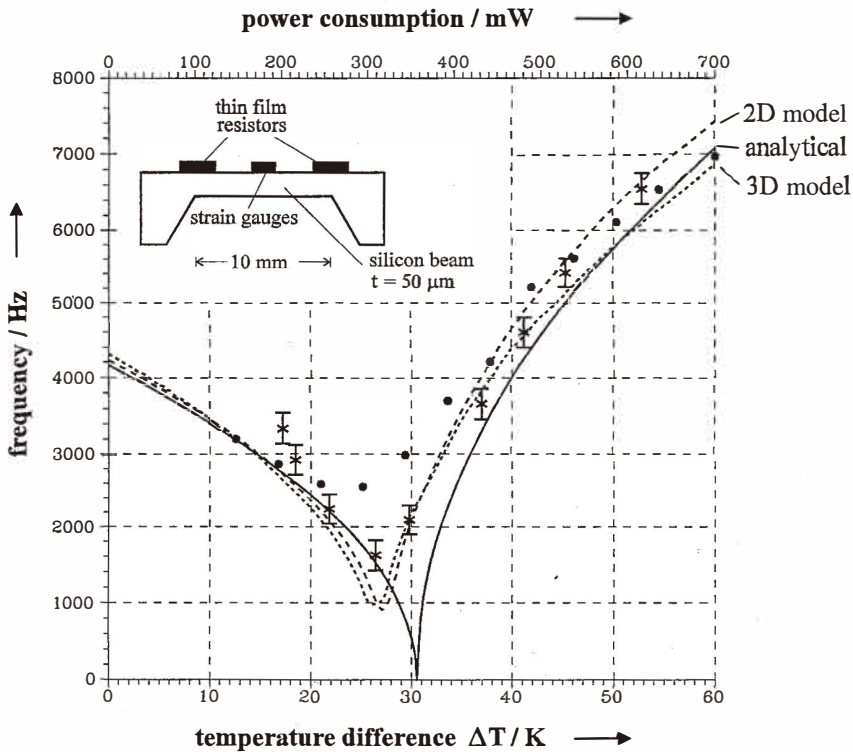


Fig. 3. Frequency-temperature characteristics of a doubly clamped silicon beam resonator. • and × denote the optically and electrically measured characteristics, respectively. The analytical curve was calculated using the model in ref. 40.

detection a laser vibrometer and an autofocus sensor were used. Power dissipation in the strain gauges causes a static average temperature rise inducing an internal stress in the beam, which results in a change in its resonance frequency. By varying the power consumption of the strain gauges, the frequency-temperature characteristic could be measured. In Fig. 3 the analytical, numerical (FEM), and experimental results are compared. For the critical temperature difference between the beam and its surroundings  $\Delta T_{cr}$ , at which the beam buckles, a value of about 27 K was determined from the finite-element models which is in good agreement with the measurements. The maximum static deflection of the beam was calculated to be 70–77  $\mu\text{m}$  in comparison to optically measured deflections between 56  $\mu\text{m}$  and 70  $\mu\text{m}$ . For  $f(\Delta T = 0)$  the 2D model yields a resonance frequency of 4223 Hz and the 3D model one of 4304 Hz. Both values are close to the measured value of 4164 Hz.

In the case of multilayer sensor structures such as piezoelectrically driven force or

pressure sensors, care has to be taken to compensate for the temperature cross-sensitivity of the resonance frequency. Several methods can be used to reduce the temperature dependence. For the resonant diaphragm pressure sensor, a temperature compensation method was investigated by finite-element modeling<sup>(37)</sup> which relies on lateral structuring of the electrodes and piezoelectric thin film areas. A reduction in the temperature cross-sensitivity of a Si-ZnO-bimorph diaphragm resonator due to lateral-layer structuring could be achieved as follows. Starting from a reference electrode configuration, which corresponds to the layout for selective mode excitation of the fundamental flexural vibration mode and which consists of a central electrode and a symmetrical four-part outer electrode driven with a phase shift of 180°, the areas of the outer electrode were decreased gradually. The final electrode configuration has a temperature dependence five times lower than that of the initial electrode configuration, that is, approximately 170 ppm/K. This result arises from the fact that by choosing a suitable layout for the ZnO areas on the silicon diaphragm, mainly bending stresses are induced by differential thermal expansion; membrane stresses, which are responsible for the resonance frequency shift, are minimized.

#### 5.4 Piezoelectric excitation

For piezoelectrically driven resonant microstructures the efficiency of the conversion from electrical to mechanical energy and vice versa is characterized by the effective electromechanical coupling factor  $k_{\text{eff}}$ , which can be approximately expressed as<sup>(42)</sup>

$$k_{\text{eff}} \approx \sqrt{\frac{f_p^2 - f_s^2}{f_p^2}}, \quad (13)$$

where  $f_p$  and  $f_s$  are the parallel and the series resonance frequencies, respectively, as derived from the electrical equivalent circuit of the piezoelectric device. In Table 2 the results of a coupled-field finite-element analysis of silicon cantilever beams uniformly covered with a ZnO thin film layer are compared to experimental data. The resonance frequency  $f_{\text{res}}$  was measured optically, while the parallel and series resonance frequencies  $f_p$  and  $f_s$ , were determined by measuring the impedance-phase characteristics of the resonant cantilever beams. The deviation between the calculated and measured values of  $k_{\text{eff}}$  of up to 52% is probably due to the residual stress in the ZnO thin films. This assumption is supported by measurements of the compressive residual stress, yielding values of up to 500 MPa.<sup>(43)</sup> In the case of ZnO layers with low residual stress (beams #4 and #5) the measured and calculated  $k_{\text{eff}}$  values agree to within a few percent, while in the case of ZnO layers with higher residual stress (beams #1, #2, and #3) the deviations between measured and calculated values are large.

Optimization of the effective electromechanical coupling factor for bimorph resonators is possible by choosing the optimum value of the thickness ratio  $t_{\text{Si}}/t_{\text{piezo}}$ . In Fig. 4, the effective coupling factors of bimorph silicon diaphragm resonators as a function of the thickness ratio are shown. Experimental data are given for ZnO thin films. The calculated curves show a maximum at  $t_{\text{Si}}/t_{\text{piezo}} = 3.5$  (AlN), 2 (ZnO), and 1.3 (PZT) corresponding to maximum coupling factors  $k_{\text{eff}}$  of 0.09, 0.22, and 0.38, respectively.

Table 2

Characteristics of silicon cantilever beams (length = 7 mm, width = 5 mm) uniformly covered with a ZnO thin film layer.

Beam no.	#1	#2	#3	#4	#5
$t_{\text{Si}}$ [ $\mu\text{m}$ ]	123.7	124.5	137.2	124.5	124.5
$t_{\text{ZnO}}$ [ $\mu\text{m}$ ]	10.4	10.1	10.7	7.75	7.75
Measurements <sup>(43)</sup>					
$f_{\text{res}}$ [Hz]	3330	3410	3680	3455	3455
$f_{\text{s}}$ [Hz]	3358	3416	3642	3418	3420
$f_{\text{p}}$ [Hz]	3376	3430	3654	3439	3445
$k_{\text{eff}}$	0.103	0.090	0.081	0.110	0.120
Finite-element modeling					
Elements	2080	2080	4410	4410	4410
Nodes	2781	2781	6144	6144	6144
$f_{\text{s}}$ [Hz]	3474	3495	3832	3474	3474
$f_{\text{p}}$ [Hz]	3502	3523	3861	3497	3497
$k_{\text{eff}}$	0.126	0.125	0.123	0.113	0.113
$\Delta k/k$ [%]	-22	-39	-52	-3	+6

A prerequisite for mode-selective excitation and detection of the vibrations is knowledge of the stress patterns on the resonator surface in order to be able to choose the appropriate electrode design. For beamlike resonators the stress patterns can be calculated analytically,<sup>(15)</sup> but in the case of diaphragms FEM must be used. Linear harmonic response analysis must be carried out in order to determine the frequency response of the resonator structure. For all-around clamped silicon diaphragms, the first flexural vibration mode shows compressive stress areas near the clamping regions and a central tensile stress area. In order to obtain mode-selective excitation of the fundamental mode, the second and higher vibration modes must be suppressed. This can be achieved by positioning electrodes according to the different stress areas (tensile/compressive) and applying opposite potentials to them.<sup>(37)</sup>

## 5.5 Resonator optimization

### 5.5.1 Mode selectivity

Due to the induced bending moment of the silicon-ZnO bimorph structure, the flexural vibrations of piezoelectrically driven doubly clamped beams are out-of-plane. To achieve

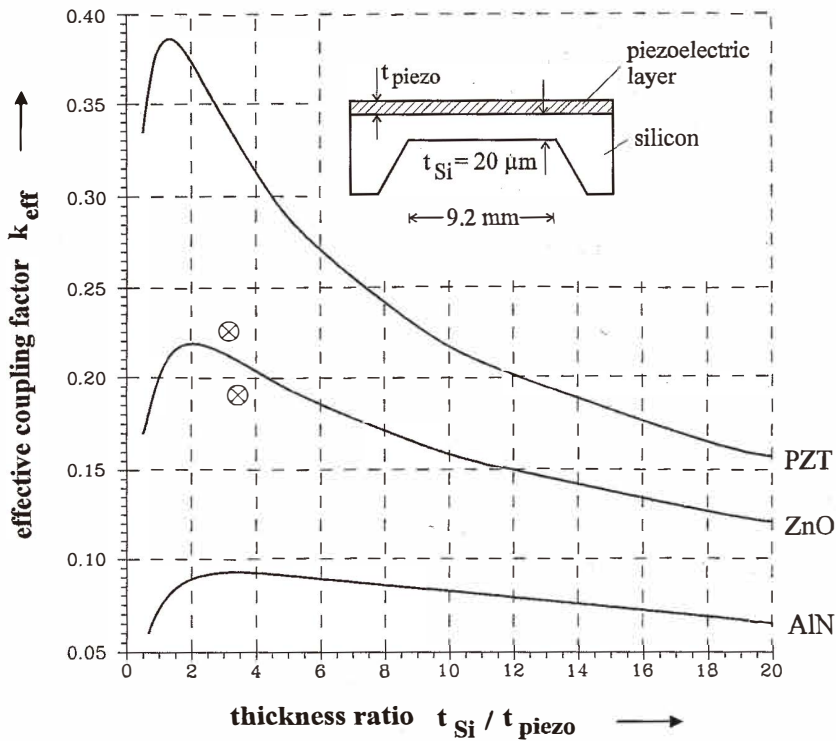


Fig. 4. Effective electromechanical coupling factors of bimorph silicon diaphragm resonators.  $\otimes$  denotes experimental values obtained for Si-ZnO-bimorph diaphragm pressure sensors.

a cancellation of moments and shear forces at the clamped ends, triple-beam<sup>(11)</sup> or quadruple-beam<sup>(12)</sup> structures are suitable. Finite-element modeling with 2D plastic shell elements has been used to simulate the dynamic behavior of a triple-beam resonator.<sup>(11)</sup> The resonator, which has a length of 3 mm, a thickness of  $20 \mu\text{m}$ , and beam widths of  $400 \mu\text{m}$  (outer beams) and  $200 \mu\text{m}$  (inner beam), is connected to the supporting bulk frame on both sides via flexible decoupling zones as indicated in Fig. 5. The thickness of the decoupling zones is equal to that of the beams, thus allowing energy transfer during vibration. The eigenfrequencies and mode shapes were determined by modal analysis, and in combination with static analysis, the frequency-force characteristic was derived. In particular, the influence of the clamping region on the degree of mechanical decoupling of the resonating structure from the supporting bulk frame was analyzed.

Figure 5 shows the dependence of the resonance frequencies of the first three flexural vibration modes on the decoupling zone length. The fundamental flexure mode of beams vibrating symmetrically in phase is denoted as M1. A spurious overtone mode M2 occurs between mode M1 and the antisymmetric sensor mode M3. Good mechanical decoupling

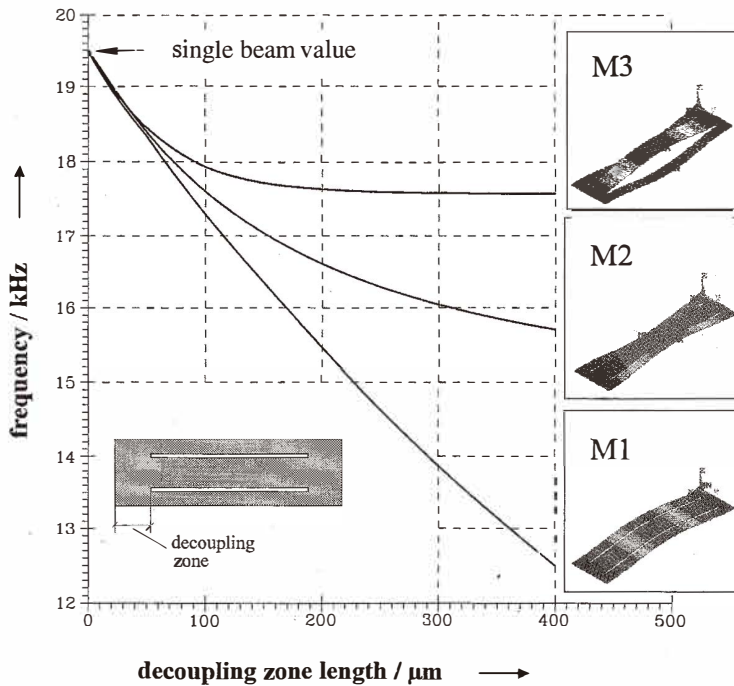


Fig. 5. Dependence of the resonance frequencies of the first three flexural vibration modes M1, M2, and M3 of a triple-beam structure on the length of the decoupling zone obtained by finite-element modeling with 2D plastic shell elements.

and sufficient splitting of the frequencies of the three vibration modes can be realized by choosing a decoupling zone length of 200–300  $\mu\text{m}$ , which has been verified experimentally.<sup>(11)</sup>

### 5.5.2 Mode decoupling

For the realization of resonant pressure sensors, microstructures consisting of a resonating beam connected at both ends to a diaphragm, known as 'beam-on-diaphragm' (BOD) structures, can be used. In such sensors, the pressure-sensitive element (diaphragm) is separated from the resonator (doubly clamped beam). In recent years several BOD pressure sensors have been realized.<sup>(7-9)</sup> Monolithic BOD microstructures can be fabricated by means of laser machining and anisotropic etching techniques.<sup>(10)</sup> The pressure-frequency characteristic for the latter device was measured by acoustic excitation and optical detection of the vibrations. In the pressure range between  $-0.8$  bar and  $+1.0$  bar the characteristic is almost linear with a sensitivity of about 4.5 kHz/bar at a beam resonance frequency of 82 kHz.

Since there are no analytical formulae available for the dynamic behavior of this



complex sensor geometry, FEM was used to predict the sensor characteristic and to analyze the influence of geometric modifications on the sensor performance.<sup>(37)</sup> A 3D model of the sensor structure was created using the solid model I-DEAS.<sup>(44)</sup> Finite-element simulations were carried out with ANSYS<sup>(35)</sup> using one quarter of the BOD structure and assuming anisotropic material properties of single-crystal silicon. For these calculations a beam length of 1.95 mm and a thickness of 42.4  $\mu\text{m}$  were assumed. The beam is located in the center of the diaphragm and clamped between two supporting piers, which are connected monolithically to the diaphragm (see inset in Fig. 6). When a pressure difference of 1 bar is applied, the maximum displacement of the diaphragm is about 1  $\mu\text{m}$ . Due to the leverage principle, stress concentration occurs in the beam resulting in a maximum tensile stress of 24.7 MPa, which is about twice that at the surface of the diaphragm.

The diaphragm thickness was varied from 50  $\mu\text{m}$  to 300  $\mu\text{m}$  while the other dimensions were kept constant. The resonance frequencies of the fundamental flexure mode of the beam ( $f_{\text{beam}}$ ) and the first antisymmetric coupled mode of the diaphragm and the beam ( $f_{\text{diaphragm}}$ ) were calculated. While the frequency of the beam mode is largely independent of the diaphragm thickness, the frequency of the diaphragm mode is approximately proportional to the thickness of the diaphragm, as shown in Fig. 6 (see also eq. (4)). At a thickness of about 130  $\mu\text{m}$  the two resonance frequencies are equal. This geometric configuration should be avoided, because the vibration energy of the beam will be transferred into the diaphragm due to mode coupling, leading to a reduction in the Q-factor.

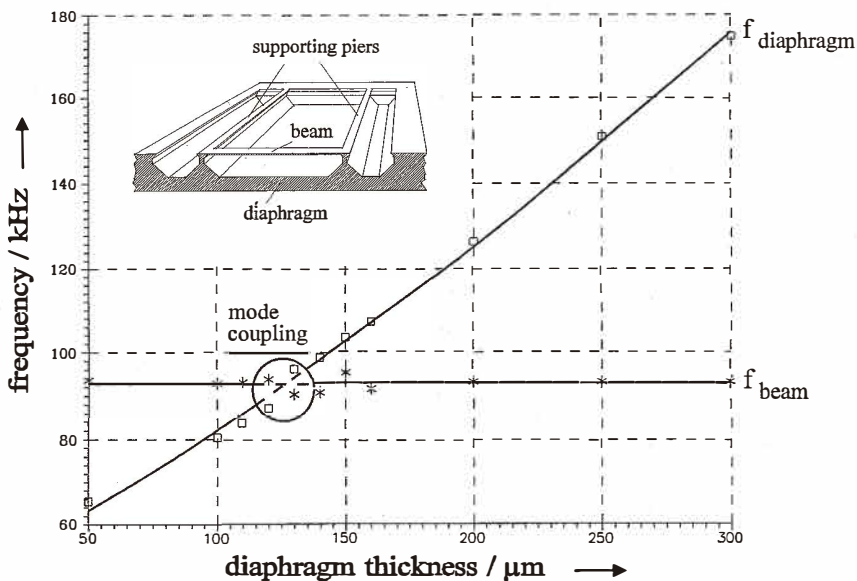


Fig. 6. Calculated resonance frequency of a BOD structure as a function of the diaphragm thickness. Beam length of 1.95 mm and thickness of 42.4  $\mu\text{m}$  were assumed. The inset shows a schematic of the BOD structure.



### 5.5.3 *Measuring range and sensitivity*

For constant beam dimensions, the pressure sensitivity varies as a function of the side length and the thickness of the diaphragm. This dependence has been calculated by FEM for a  $1\text{ mm} \times 120\text{ }\mu\text{m} \times 42.4\text{ }\mu\text{m}$  resonating doubly clamped beam and  $300\text{-}\mu\text{m}$ -thick diaphragms with side lengths between 2.5 mm and 5 mm. The calculated pressure sensitivities vary from 0.5 kHz/bar to 11 kHz/bar.

By reducing the side length, the measuring range of the sensor can be enhanced. For example, the fundamental resonance frequency of a diaphragm with a side length of 2 mm has been calculated to be 386 kHz. The pressure sensitivity is about 141 Hz/bar in the pressure range between 0 and 100 bar. At the maximum pressure difference of 100 bar, a tensile stress of 60 MPa arises in the beam.

These calculations demonstrate that by variation of the dimensions of a BOD structure, sensors for a wide pressure range can be fabricated.

## 6. Conclusion

In order to optimize the performance of resonant silicon microsensors, knowledge of their internal behavior is necessary. To achieve this in a reasonable time, modeling and numerical simulation are necessary. For simple resonator structures with ideal boundary conditions, analytical models may be used to calculate their characteristics accurately if homogeneous and isotropic material behavior is assumed.

For more complex resonator structures, arbitrary boundary conditions, anisotropic and temperature-dependent material properties, and in the presence of coupled-field effects, FEM can be used to simulate the properties of resonant microstructures. Beamlike force and diaphragm pressure sensors as well as triple-beam and beam-on-diaphragm microstructures have been used to demonstrate the capability of this method to calculate eigenfrequencies, mode shapes, load-dependent frequency changes and cross-sensitivities, as well as to optimize the resonator geometry with respect to mode selectivity, mode decoupling, electromechanical coupling efficiency, and measuring range and sensitivity.

These examples clearly demonstrate that finite-element modeling is an indispensable tool for the development of complex resonant microstructures as well as for development of the active multilayer structures used to excite the vibrations.

## Acknowledgments

This work was partially supported by the Bundesministerium für Forschung und Technologie under contract number 13 AS 0114.

## References

- 1 G. Stemme: Resonant silicon sensors, *J. Micromech. Microeng.* **1** (1991) 113.
- 2 H. A. C. Tilmans, M. Elwenspoek and J. H. J. Fluitman: Micro resonant force gauges, *Sensors and Actuators A* **30** (1992) 35.
- 3 R. A. Buser: Resonant Sensors, in: *Sensors*, Vol. 7, *Mechanical Sensors*, ed. H. H. Bau, N. F. de Rooij and B. Kloeck (VCH, Weinheim, 1994) p. 205.
- 4 S. Büttgenbach: *Mikromechanik* (Teubner, Stuttgart, 1991).
- 5 J. C. Greenwood and D. W. Satchell: Miniature silicon resonant pressure sensor, *IEE Proceedings* **135** (1988) 369.
- 6 K. Ikeda, H. Kuwayama, T. Kobayashi, T. Watanabe, T. Nishikawa, T. Yoshida and K. Harada: Silicon pressure sensor integrates resonant strain gauge on diaphragm, *Sensors and Actuators A* **21–23** (1990) 146.
- 7 K. E. B. Thornton, D. Uttamchandani and B. Culshaw: A sensitive optically excited resonator pressure sensor, *Sensors and Actuators A* **24** (1990) 15.
- 8 R. A. Buser, L. Schultheis and N. F. de Rooij: Silicon pressure sensor based on a resonating element, *Sensors and Actuators A* **25–27** (1991) 717.
- 9 K. Petersen, F. Pourahmadi, J. Brown, P. Parsons, M. Skinner and J. Tudor: Resonant silicon beam pressure sensor fabricated with silicon fusion bonding, *Proc. 6th Int. Conf. Solid-State Sensors and Actuators (Transducers '91)*, San Francisco, 1991, p. 664.
- 10 A. Schumacher, M. Alavi, Th. Fabula, B. Schmidt and H. -J. Wagner: Monolithic bridge-on-diaphragm microstructure for sensor applications, *Proc. Micro System Technologies 94*, Berlin, 1994, p. 309.
- 11 Th. Fabula, H. -J. Wagner, B. Schmidt and S. Büttgenbach: Triple-beam resonant silicon force sensor based on piezoelectric thin films, *Sensors and Actuators A* **41–42** (1994) 375.
- 12 H. A. C. Tilmans: Micro-mechanical sensors using encapsulated built-in resonant strain gauges, Ph.D. thesis (University of Twente, Enschede, 1993).
- 13 K. J. Bathe: *Finite-element procedures in engineering analysis* (Prentice Hall Inc., Englewood Cliffs, 1982).
- 14 J. G. Smits, H. A. C. Tilmans, K. Hoen, H. Mulder, J. van Vuuren and G. Boom: Resonant diaphragm pressure measurement system with ZnO on Si excitation, *Sensors and Actuators* **4** (1983) 565.
- 15 A. Prak: Silicon resonant sensors: operation and response, Ph. D. thesis (University of Twente, Enschede, 1993).
- 16 W. Weaver, S. P. Timoshenko and D. H. Young: *Vibration problems in engineering* (John Wiley, New York, 1990).
- 17 S. Bouwsra and B. Geijselaers: On the resonance frequencies of microbridges, *Proc. 6th Int. Conf. Solid-State Sensors and Actuators (Transducers '91)*, San Francisco, 1991, p. 538.
- 18 S. P. Timoshenko and S. Woinowsky-Krieger: *Theory of plates and shells* (McGraw-Hill, New York, 1987).
- 19 D. Young: Vibration of rectangular plates by the Ritz method, *J. Appl. Mech.*, Dec. (1950) 448.
- 20 R. D. Blevins: *Formulas for natural frequency and mode shapes* (Krieger, Malabar, 1984).
- 21 P. Pons and G. Blasquez: Natural vibration frequencies of silicon diaphragms, *Proc. 6th Int. Conf. Solid-State Sensors and Actuators (Transducers '91)*, San Francisco, 1991, p. 543.
- 22 D. Uttamchandani, K. E. B. Thornton, J. Nixon and B. Culshaw: Optically excited resonant diaphragm pressure sensor, *Electron. Lett.* **23** (1987) 152.
- 23 Th. Fabula and A. Schroth: Simulation des dynamischen Verhaltens mikromechanischer Membranen, *VDI-Berichte 960* (VDI, Düsseldorf, 1992).

- 24 H. L. Chau and K. D. Wise: Scaling limits in batch-fabricated silicon pressure sensors, *IEEE Trans. Electron Devices* **ED-34** (1987) 850.
- 25 W. Weizel: *Lehrbuch der theoretischen Physik*, Band I (Springer, Berlin, 1963).
- 26 D. Braess: *Finite Elemente* (Springer, Berlin, 1991).
- 27 P. G. Ciarlet: *The finite-element method for elliptical problems* (North-Holland, Amsterdam, 1978).
- 28 A. Matzenmiller and W. Rust: *ANSYS-Seminar Notes: Nonlinearities* (CADFEM GmbH, Grafing, 1993).
- 29 P. Kohnke (ed.): *ANSYS User's Manual for Revision 5.0, Volume IV, Theory* (ANSYS, Inc., Houston, 1992).
- 30 C. C. Rankin and F. A. Brogan: An element independent corotational procedure for the treatment of large rotations, *J. Pressure Vessel Techn.* **108** (1986) 165.
- 31 H. Allik and T. J. R. Hughes: Finite-element method for piezoelectric vibration, *Int. J. Numerical Methods in Engineering* **2** (1970) 151.
- 32 L. D. Clayton, S. R. Swanson and E. P. EerNisse: Modifications of the double-ended tuning fork geometry for reduced coupling to its surroundings: finite-element analysis and experiments, *IEEE Trans. Ultrasonics, Ferroelect., Freq. Control* **UFFC-34** (1987) 243.
- 33 S. P. Beeby and M. J. Tudor: Modelling and optimization of micromachined silicon resonators, *Techn. Digest, Micromechanics Europe '94, Pisa, 1994*, p. 44.
- 34 M. Alavi, Th. Fabula, A. Schumacher and H. -J. Wagner: Monolithic microbridges in silicon using laser machining and anisotropic etching, *Sensors and Actuators A* **37-38** (1993) 661.
- 35 ANSYS, Inc., Houston, USA.
- 36 Landolt-Börnstein: *Zahlenwerte und Funktionen aus Naturwissenschaft und Technik*, Gruppe III, Band **17a** (Springer, Berlin, 1982).
- 37 Th. Fabula: *Dynamisches Verhalten mikromechanischer Strukturen-Finite Elemente Simulation zur Entwurfsunterstützung und deren meßtechnische Verifikation*, Ph.D. thesis (University of Bonn, 1994).
- 38 G. J. Tjhuis: *Onderzoek naar het druk-frequentie verband van een resonerende membraan druksensor*, Diploma thesis (University of Twente, Enschede, 1987), in Dutch.
- 39 Th. Fabula: *Dynamische Berechnungen in der Mikromechanik-Simulation/Messung*, Proc. 10. ANSYS User's Meeting, Arolsen (CADFEM GmbH, Grafing, 1992).
- 40 H. J. M. Geijselaers and H. Tjeldeman: The dynamic mechanical characteristics of a resonating microbridge mass-flow sensor, *Sensors and Actuators A* **29** (1991) 37.
- 41 Th. Fabula, N. Hey and S. Messner: *Gekoppelte Feldberechnung eines mikromechanischen Strömungssensors*, Proc. 11. CADFEM Users' Meeting, Bamberg (CADFEM GmbH, Grafing, 1993).
- 42 R. Lerch: Simulation of piezoelectric devices by two- and three-dimensional finite elements, *IEEE Trans. Ultrasonics, Ferroelect., Freq. Control* **UFFC-37** (1990) 233.
- 43 G. Flik: private communication.
- 44 Structural Dynamics Research Corporation, Milford, USA.